



Spatiotemporal patterns of temperature inversions and impacts on

2 surface PM_{2.5} across China

- 3 Yonglin Fang¹, Hancheng Hu¹, Xiangdong Zheng², Jianping Guo³, Xingbing Zhao⁴, Fang Ma⁵, Hao Wu¹
- 4 ¹College of Electronic Engineering & Key Laboratory of CMA Atmospheric Sounding, Chengdu University of Information
- 5 Technology, Chengdu 610225, China
- 6 ²Chinese Academy of Meteorological Sciences, Beijing 100081, China
- 7 3State Key Laboratory of Severe Weather Meteorological Science and Technology & Specialized Meteorological Support
- 8 Technology Research Center, Chinese Academy of Meteorological Sciences, Beijing 100081, China
- 9 ⁴Chengdu Institute of Plateau Meteorology, China Meteorological Administration, Chengdu 610072, China
- 10 ⁵Yunnan Atmospheric Observation Technology Support Center, Kunming 650034, China
- 11 Correspondence: Hao Wu (wuhao@cuit.edu.cn)
- 12 Abstract. Temperature inversions (TIs) strongly regulate the accumulation and dispersion of air pollutants, yet their
- 13 nationwide impacts on surface PM_{2.5} remain poorly quantified. Here we integrate high-resolution L-band radiosonde profiles
- with PM_{2.5} monitoring data from 2016–2021 to characterize the frequency, intensity, thickness, and diurnal variability of TIs—
- 15 including surface-based inversions (SBIs) and elevated inversions (EIs)—across mainland China. We show that TIs are
- 16 pervasive, occurring on average 52% of days, with mean strength of 2.1 °C and thickness of 214 m, and are more common at
- 17 08:00 than 20:00. Distinct regional patterns emerge: SBIs dominate in northern China and are 1.3 °C stronger than EIs, whereas
- 18 Els prevail in the east and are ~16 m thicker. Tls intensify seasonal pollution, with 76% of PM_{2.5} episodes coinciding with
- 19 inversion events. SBI strength correlates positively with PM_{2.5} concentrations nationwide, while EI parameters show negative
- 20 associations in eastern and southern regions. These findings reveal the spatiotemporal dynamics of TIs, establish quantitative
- 21 links to surface pollution, and highlight regionally divergent mechanisms, providing critical insight for air-quality forecasting
- and targeted emission control.
- 23 **Keywords:** Temperature inversion, PM_{2.5}, Air pollution, Radiosonde profiles.

24 1 Introduction

- 25 Fine particulate matter (PM_{2.5}, aerodynamic diameter ≤ 2.5 μm) is a dominant component of atmospheric aerosols and a major
- driver of air pollution in China (Liang et al., 2021; Luo et al., 2024; Yan et al., 2023; Zang et al., 2021). Over the past two
- decades, recurrent severe haze episodes characterized by elevated PM_{2.5} levels have imposed substantial public health burdens,
- 28 including respiratory, cardiovascular, and reproductive impairments, as well as increased cancer risk (Chan and Yao, 2008;
- 29 Yan et al., 2021; Garcia et al., 2023; Rentschler and Leonova, 2023; Zuo et al., 2023; Chen et al., 2025). In response, stringent
- 30 emission control policies since 2013 have markedly improved air quality, with annual mean PM_{2.5} concentrations declining





32

33

34

35

36

37

38

39

40

41

42

43

44

45

46

47

48

49

50

51

52

53

54

55

56

57

58

59

60

61

62

from 68 μg m⁻³ in 2013 to 29 μg m⁻³ in 2022 (Meng et al., 2023; Peng et al., 2025; Zou et al., 2025). Nevertheless, seasonal pollution episodes remain acute, particularly in the Beijing-Tianjin-Hebei (BTH) region, where the 2022 annual mean still reached 44 μg m⁻³ (Ministry of ecology and environment the people's republic of China, 2022), exceeding the World Health Organization's Stage-1 interim target of 35 µgm⁻³ (WHO, 2021). Growing evidence shows that such extreme events are not solely determined by anthropogenic emissions but are strongly modulated by adverse meteorological conditions, among which temperature inversion (TI) plays a pivotal role (Feng et al., 2020; Morawska et al., 2021; Deng et al., 2022; Shao et al., 2023; Sun et al., 2025). In meteorology, TI refers to the anomalous increase of temperature with altitude, most frequently observed in the lower troposphere. TIs arise through multiple mechanisms, including nocturnal radiative cooling, warm-air advection, topographic confinement, and subsidence warming under high-pressure system (Vihma et al., 2011; Kassomenos et al., 2014; Largeron and Staquet, 2016; Xu et al., 2019). Surface-based inversions (SBIs) typically form at night when radiative cooling produces a shallow, stable layer of cold air near the surface, which usually dissipates after sunrise or under strong winds (>20 km h⁻¹). In contrast, elevated inversions (EIs) are driven by synoptic-scale processes such as warm advection over cooler surfaces, subsidence within anticyclonic systems, or frontal overrunning (Czarnecka et al., 2019; Huang et al., 2021; Palarz et al., 2018). The presence of a temperature inversion (TI) suppresses turbulent mixing, strengthens atmospheric stability, and traps pollutants near the surface (Kahl, 1990; Zhong et al., 2018). Within the boundary layer, this stable stratification creates a pronounced "capping effect" that critically limits vertical pollutant dispersion (Stull, 1988). The resulting suppression of pollutant ventilation operates through three interconnected mechanisms. First, the inversion layer itself acts as a meteorological cap, inhibiting vertical mixing and fostering rapid near-surface accumulation of aerosols (Zhong et al., 2017). Second, synoptic conditions conducive to inversion formation-particularly for surface-based inversions-are often accompanied by weak horizontal winds, further restricting advective transport (Yang and Shao, 2021). Third, the persistence of inversions, especially under wintertime high-pressure systems, prolongs pollution episodes over multiple days, allowing progressive buildup of PM2.5 and compounding air quality deterioration (Feng et al., 2020). Collectively, these processes establish TIs as a pivotal meteorological driver of severe pollution across diverse regions. Extensive research over the past two decades has examined the characteristics of temperature inversions (TIs) and their interactions with air pollution (Rendón et al., 2015; Wolf et al., 2014; Wu et al., 2014; Yin et al., 2021). Early studies highlighted their synoptic controls: Milionis and Davies (1992) identified upper-level inversions between 950-800 hPa over Hemsby, UK, primarily associated with subsidence within anticyclonic systems. At a continental scale, Zhang et al. (2011) analyzed radiosonde data from 50 U.S. stations and showed that lower-tropospheric inversions (LTIs) are widespread, with strong zonal wind shear playing a key role in their formation. More recently, advanced remote sensing has enabled quantitative assessment of inversion-aerosol interactions. For example, Liu et al. (2022) combined lidar and radiosonde measurements over the Southern Great Plains to demonstrate that inversion intensity critically determines the aerosol-trapping capacity of the

https://doi.org/10.5194/egusphere-2025-4751 Preprint. Discussion started: 28 October 2025 © Author(s) 2025. CC BY 4.0 License.



63

64

65

66

67

68

69

70

71

72

73

74

75

76

77

78

79

80

81

82

83

84

85

86

87

88

89

90

91

92

specific air quality forecasting and management.



boundary layer.

Nonetheless, most existing studies remain limited to individual cities or specific regions. For example, Wallace et al. (2009) showed that nocturnal inversions in Hamilton, Canada increased PM2.5 concentrations by 54%, with mobile observations further revealing the reinforcing role of local topography in inversion formation and pollutant buildup. In China, Xu et al. (2019) reported that 93% of heavy pollution episodes in Beijing coincided with inversion conditions, while Feng et al. (2020) found that winter inversions in the Sichuan Basin elevated PM_{2.5} levels by 64.7% compared with non-inversion days. Beyond China, Lagmiri and Dahech (2024) identified inversions as the dominant driver of particulate pollution in Cergy-Pontoise, France, with nearly 80% of PM₁₀ exceedances occurring under inversion conditions persisting 1-3 days in winter. Structural analyses have also revealed multi-layer inversion systems: Li et al. (2012) described a four-tiered inversion structure over central China, linking mid-tropospheric inversions to synoptic cold fronts and regional advection, while upper-level inversions exhibited strong latitudinal dependence. While these studies underscore the critical role of inversions in pollution accumulation, substantial knowledge gaps remain regarding their nationwide patterns and interactions with PM2.5 across China's diverse climatic and topographic settings. The country's complex geography—spanning plains, basins, and plateaus—produces pronounced regional heterogeneity in inversion mechanisms and vertical structures (Yang et al., 2025). For instance, the North China Plain is frequently subjected to strong wintertime SBIs, whereas the Sichuan Basin is characterized by deep, persistent inversions confined by topography (Guo et al., 2020; Huang et al., 2021; Xu et al., 2021). Such spatial variability drives region-specific impacts on PM_{2.5} accumulation, underscoring the need for systematic, high-resolution observational analyses. Although Yang and Shao (2021) documented a nationwide increase in inversion frequency over the past three decades using reanalysis products, the coarse vertical resolution of datasets such as ERA5 (25 hPa layers) hampers accurate representation of inversion structure. Similarly, radiosonde-based studies (Guo et al., 2020; Huang et al., 2021; Xu et al., 2021) have provided valuable regional insights but fall short of offering a comprehensive national-scale assessment of boundary-layer inversions and their impacts on PM2.5 pollution. In this study, we employ high-vertical-resolution radiosonde observations (6-8 m) from 2016 to 2021 to accurately detect inversion layers and their vertical structures, thereby overcoming the coarse limitations of reanalysis data. By integrating these measurements with nationwide PM2.5 monitoring records from the Ministry of Ecology and Environment, we systematically characterize the spatiotemporal distribution of temperature inversions across China, quantify the distinct impacts of SBI and EI on surface PM_{2.5} concentrations, and establish dynamic relationships between inversion parameters and pollution levels. These findings provide new mechanistic insight into inversion-pollution interactions and offer scientific support for region-





2 Study area and Data

2.1 Study area

Our analysis covers mainland China, a region of vast spatial extent and pronounced physiographic complexity where monsoonal and continental regimes interact to produce strong environmental heterogeneity. To capture this diversity, we partition the domain (excluding Hong Kong, Macau, and Taiwan owing to data limitations) into seven regions based on integrated meteorological characteristics and major urban agglomerations (Fig. 1). The Northeast (NE)—a traditional industrial base with cold, dry winters—features emissions dominated by coal-fired heating and heavy industry. North China (NC), including the Beijing—Tianjin—Hebei megacity cluster, is characterized by dense population, intensive industrial and vehicular activity, and frequent severe haze. The Northwest (NW) comprises plateaus, basins, and deserts under a continental climate with strong insolation and large diurnal temperature ranges; dust and energy/chemical sectors are major contributors. East China (EC) and South China (SC) lie in the East Asian monsoon zone and are among the most economically active regions, influenced by industrial and traffic emissions and regional transport. The Southwest (SW)—spanning the Tibetan Plateau, the Yunnan—Guizhou Plateau, and the Sichuan Basin—is the most topographically and climatically diverse, where topographic confinement and local circulations strongly modulate pollution composition and evolution.

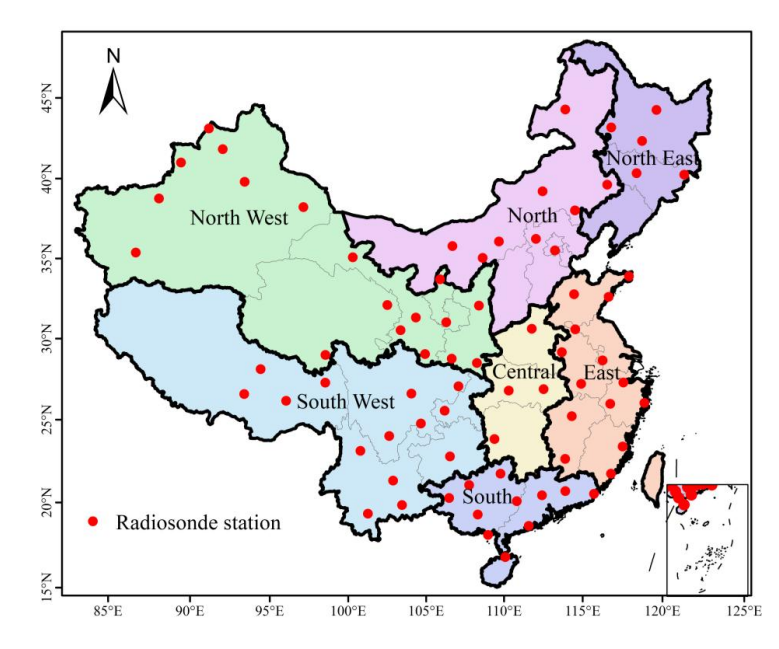


Fig.1 Distribution of 75 radiosonde stations in China. The inset map in the lower right shows the South China Sea Islands.

2.2 Data

Radiosonde observations. We use L-band high-resolution sounding data from the operational network of the China Meteorological Administration (CMA). Since nationwide deployment in 2011, the system has routinely operated ~120



115

116

117

118

119

120

121

122

123

124125

126

127

128

129

130

131

132

133

134

135

136

137

138

139

140

141

142



radiosonde stations with standard launches at 08:00 and 20:00 Beijing Time (00:00 and 12:00 UTC), with additional warmseason soundings (May-August) to capture monsoon processes (Guo et al., 2016; Yan et al., 2020). The GTS1 digital radiosonde provides vertical profiles of temperature, pressure, humidity, wind speed and direction from the surface to ~30 km, with 5-8 m nominal vertical resolution (sampling frequency 1.2 s). Independent assessments indicate temperature errors <0.1 K in the troposphere and data quality comparable to internationally recognized radiosondes within the planetary boundary layer (Ma et al., 2010). These measurements have been widely applied to studies of cloud microphysics, PBL height, and inversion detection, and as inputs to numerical weather prediction and atmospheric composition research (Li et al., 2019; Zang et al., 2017; Zhang et al., 2020). For this study (2016-2021), we applied routine quality control to remove obvious temperature/height outliers and used the full-resolution vertical profiles to identify inversion layers and derive their properties. Surface PM_{2.5} monitoring. Hourly PM_{2.5} concentrations were obtained from the national air-quality monitoring network operated by the China National Environmental Monitoring Centre (CNEMC; real-time platform: https://www.cnemc.cn/en/) (Miao et al., 2020; Yan et al., 2020). As of 1 March 2022, the network comprised 2,026 stations with dense coverage in eastern urban clusters and relatively sparse representation in western high-altitude regions. To match radiosonde stations with PM_{2.5} monitors, we used a distance threshold method with a 10 km search radius. This approach identified 75 valid station pairs, balancing spatial representativeness and sample size (Fig. 1). The 10 km threshold avoids underrepresentation from smaller radii and minimizes spatial error from larger distances, representing the point where further increases yield diminishing returns in matches (the specific screening method is shown in Fig. S1). For temporal alignment with the soundings, hourly PM2.5 records were extracted around 08:00 and 20:00 BJT. Basic completeness checks and standard plausibility screening were applied before analysis. Rationale for integration. The combination of meter-scale-resolution vertical thermodynamic profiles with collocated surface PM_{2.5} enables a consistent, observation-based assessment of inversion frequency, intensity, and thickness—and their diurnal and regional variability—while overcoming the coarse vertical structure inherent in reanalysis products .(Li et al., 2019; Yan et al., 2020; Zhang et al., 2020)

3 Method

The sounding data underwent manual quality control to identify and systematically remove obvious errors in temperature and height measurements. Raw temperature profiles were first interpolated using cubic splines to ensure vertical continuity. TIs were then identified by applying a first-derivative algorithm to the smoothed profiles (Kahl, 1990; Serreze et al., 1992). Each profile was scanned upward from the surface; layers exhibiting a positive vertical temperature gradient were classified as inversion layers, while those with negative gradients were considered non-inversion zones. The base height of an inversion layer was defined as the lowest altitude at which temperature began to increase with height, and the top height was identified





as the point where the gradient reverted to negative. Following Kahl et al. (1996), three fundamental TI parameters were derived: inversion thickness (ΔH), inversion strength (ΔT), inversion frequency (F_{TI}). They are defined as:

$$\Delta H = H_t - H_b \tag{1}$$

$$\Delta T = T_t - T_b \tag{2}$$

$$F_{TI} = N_{TI}/N \tag{3}$$

$$F_{SBI} = N_{SBI}/N \tag{4}$$

$$F_{EI} = N_{EI}/N \tag{5}$$

where H_t and H_b represent the top and bottom heights of the temperature inversion layer respectively; T_t and T_b represent the temperatures at the top and bottom respectively; N represents the total number of detections, N_{TI} represents the number of detections where temperature inversion occurs, and N_{SBI} and N_{EI} represent the number of detections where SBI and EI occur respectively.

To mitigate false positives from small-scale turbulence (e.g., "sawtooth" noise in balloon-borne measurements), thresholds for ΔH and ΔT were imposed per established practices (Guo et al., 2020; Kahl, 1990). A layer was classified as a valid TI only if $\Delta H \geq 100$ m and $\Delta T \geq 0.5$ °C; otherwise, it was discarded. Non-inversion layers embedded within broader TIs were permitted, provided the overarching TI met these criteria. Inversion can also be classified into SBI and EI based on the base height. When $H_b < 100$ m, it is called Surface-based inversions (SBIs); when 100 m $< H_b \leq 2000$ m, it is called Elevated inversions (EIs). Theoretical calculations indicate that each station should have a total of 4384 soundings at 12-hour intervals from 2016 to 2021. In practice, however, data omissions occurred due to various factors, resulting in an average missing rate of 3.2% for temperature inversion data in the final statistics.

According to China's National Ambient Air Quality Standards (GB3095-2012), a pollution event is defined when the $PM_{2.5}$ concentration exceeds 75 μ g m⁻³. $PM_{2.5}$ concentrations are further classified into six categories: Excellent: 0-35 μ g m⁻³; Good: 35-75 μ g m⁻³; Light pollution: 75-115 μ g m⁻³; Moderate pollution: 115-150 μ g m⁻³; Severe pollution: 150-250 μ g m⁻³; Extreme pollution: >250 μ g m⁻³. To align with the spatiotemporal characteristics of the radiosonde data, the hourly $PM_{2.5}$ data were processed into two time periods corresponding to the radiosonde observations: 08:00 and 20:00 Beijing Time.

4 Results and Discussions

4.1 Spatiotemporal distribution of atmospheric temperature inversions in China

The base height of a temperature inversion (TI) sets the effective lid for vertical pollutant dispersion. To resolve its vertical structure within the boundary layer, we quantified the vertical distribution of inversion events. This is defined as the percentage of the total number of inversion events falling within each 200-m height bin from the surface to 2 km (Fig. 2). A distinct non-linear profile emerges: TI proportion peaks at 27.5% near the surface (0–200 m), declines sharply to a minimum of 6.4% at





600-800 m, and then gradually increases to 10.0% at 1,800-2,000 m—i.e., a "rapid decline, then slow recovery" with height.

Marked regional contrasts accompany this vertical pattern. In the near-surface layer (0–200 m), the Southwest exhibits the highest TI proportion (36.0%), followed by northern regions—Northeast, North, and Northwest China (mean 34.7%). In comparison, Central, East, and South China show lower near-surface inversion proportion, with South China the lowest (14.1%). The pattern reverses aloft: for elevated inversions (1,800–2,000 m), South China records the highest proportion (12.5%), whereas northern regions are much less affected, reaching a minimum in North China (7.0%). Taken together, near-surface inversions preferentially occur over inland northern and southwestern China, while elevated inversions are more common in the southeastern coastal belt. A plausible driver of this dipole is the diurnal temperature range (DTR): larger DTRs over inland northern and southwestern regions enhance nocturnal radiative cooling, favoring shallow, surface-based inversions; weaker DTRs in maritime-influenced southeastern areas favor synoptic processes that produce elevated inversions.

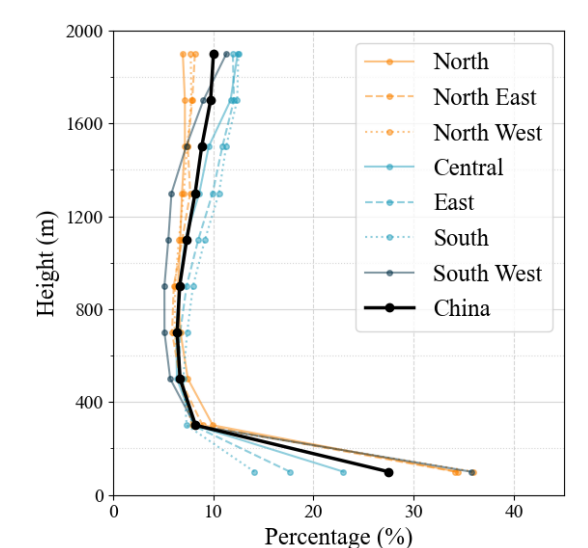


Fig.2 Vertical distribution of inversion base height: fraction of total inversions per height bin.

4.1.1 Inversion frequency

Figure 3 maps the spatial and seasonal variability of TI frequency over China (2016–2021), revealing pronounced regional heterogeneity. High TI occurrence is concentrated along the coasts (East and South China) and across northern China (Northeast, North, Northwest), yielding a national annual mean of 54.9%. Northeast China records the highest frequency (59.5%), whereas the Southwest is lowest (31.3%; Table 1). The suppressed occurrence in the Southwest likely reflects two factors: (i) in the Sichuan Basin the dominant signal is lower-tropospheric inversions (LTIs) that often peak above the boundary-layer depths emphasized here, and (ii) plateau climate conditions—high elevation, strong solar radiation, low air

https://doi.org/10.5194/egusphere-2025-4751 Preprint. Discussion started: 28 October 2025 © Author(s) 2025. CC BY 4.0 License.





density, and frequent strong winds linked to the westerly jet—enhance turbulent mixing and disrupt inversion persistence (Feng et al., 2020; Schiemann et al., 2009). Elevated inversions (EIs) dominate total events nationally. The two inversion types exhibit contrasting geography: SBIs cluster over northern China (Northeast, North, Northwest) with annual frequencies of 14.9–15.8%, whereas EIs prevail across the southeastern coastal and central regions (South, East, Central China), averaging 48.1% and peaking at 51.6% in East China. This spatial dipole aligns with previous radiosonde climatologies, which report more frequent SBIs in northern/western China and EI dominance in the south and east (Huang et al., 2021).

Figure 4a shows pronounced seasonality in TI occurrence. The highest monthly means occur at 08:00 BJT in January (84.0%) and at 20:00 BJT in December (68.8%), whereas minima appear in June (31.9%) and August (32.0%). National averages by type indicate SBIs ~13% and EIs ~43% annually (Figs. 4d, 4g). SBI occurrence peaks in February, March, September, and October (all >24%), while EI frequency maximizes in January (75.2%). Seasonal contrasts are stark: inversions are most frequent in the cold season and relatively rare in the warm season. The spatial footprint of inversion-prone areas expands westward from summer to winter: in summer, only the Northeast exceeds 40%, and the Southwest falls to 17.5%; in winter, all regions except the Southwest surpass 70%, reaching 80.5% in the Northeast. SBIs and EIs share this seasonal phasing—winter maxima, summer minima—consistent with longer winter nights that enable sustained radiative cooling and stronger stability. A persistent "east-high, west-low" gradient is also evident. One contributing factor is the fixed launch time relative to local solar time: China spans roughly five time zones, so the 08:00 BJT sounding corresponds to ~05:00 local time in the far west, when nocturnal inversions may not yet have fully developed, biasing frequencies lower there.

Further analysis (Figs. S2, 4a) shows a robust dawn–dusk asymmetry: inversions are more likely at 08:00 BJT across all regions and seasons, with daytime launches accounting for 62% of all TI detections. The contrast is strongest in summer, when 08:00 inversions comprise 71% of events, and weaker in winter (57%). This seasonal modulation reflects differences in solar forcing. In summer, long days and short nights curtail both the formation window and stability of inversions: with sunrise near 05:20 BJT, 2–3 hours of insolation have already eroded the nocturnal layer by 08:00, and by 20:00 roughly 12 hours of high-angle solar heating have largely dissipated residual stability—yielding a 26.4% frequency gap between the two launch times. In winter, short days and long nights promote deeper, more persistent inversions: with sunrise around 07:20 BJT, less than an hour of weak insolation precedes the 08:00 sounding, and the subsequent ~10 hours of low-angle daylight only modestly disturb the surface layer before 20:00. Consequently, the 08:00–20:00 difference contracts to 14.8% in winter.





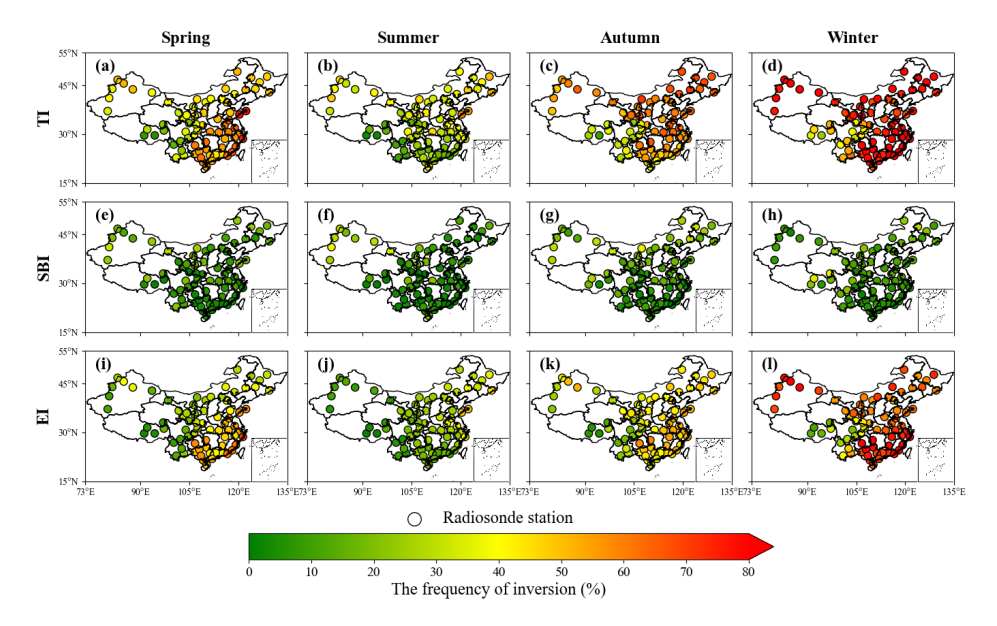


Fig. 3. Spatial and seasonal distribution of occurrence frequency for different types of TI.

221

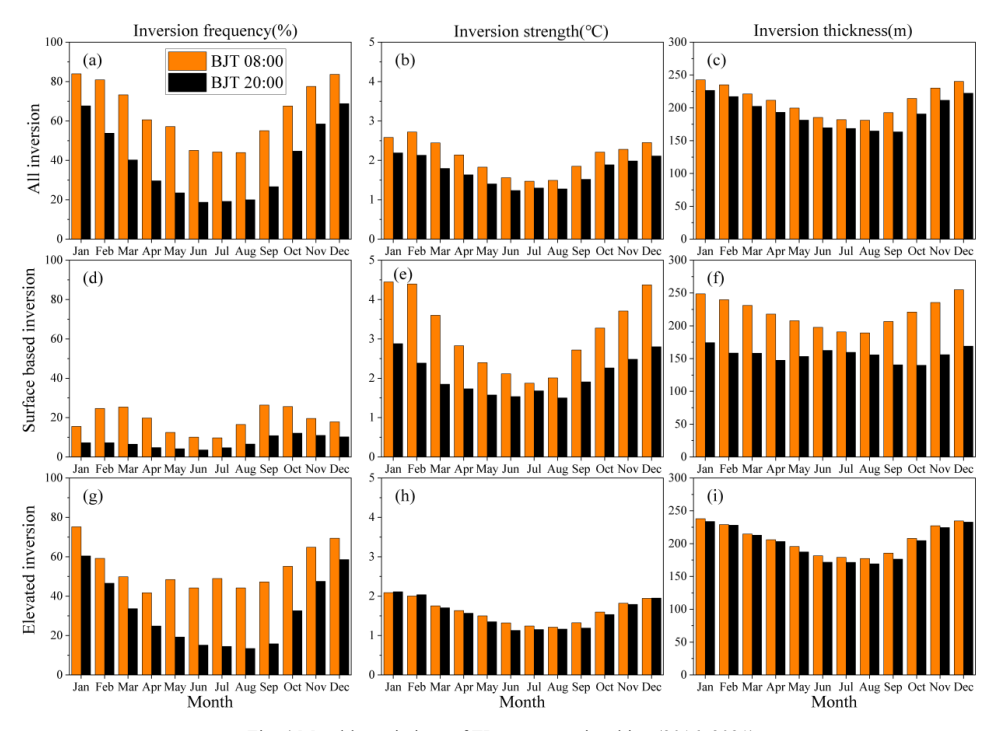


Fig. 4 Monthly variations of TI parameters in China (2016–2021).

224225

226





Table 1. Annual mean values of TI parameters by region.

Region	TI			SBI			EI		
	$F_{TI}(\%)$	Δ <i>T</i> (°C)	ΔH(m)	$F_{SBI}(\%)$	Δ <i>T</i> (°C)	ΔH(m)	$F_{EI}(\%)$	Δ <i>T</i> (°C)	ΔH(m)
Central	57.0	2.08	231	10.0	3.54	213	47.0	1.80	235
East	59.3	1.86	217	7.7	2.54	197	51.6	1.74	219
North	55.8	2.20	201	14.9	3.72	204	40.9	1.63	199
North East	59.5	2.11	211	16.1	3.34	210	43.4	1.63	212
North West	49.3	2.67	215	15.8	3.91	209	33.5	1.92	218
South	50.7	1.92	222	5.0	1.74	186	45.7	1.93	227
South West	31.3	2.05	202	9.6	2.39	186	21.7	1.66	202

4.1.2 Inversion strength

The TIs exerts first-order control on pollutant dispersion. Spatially, TI strength is greater over inland northern regions than over southern and eastern coasts (Fig. 5; Table 1): the Northwest has the highest annual mean (2.67 °C), whereas the East is lowest (1.86 °C). Extremes span 4.69 °C in the Southwest to 1.67 °C in the East. Seasonally, TI strength peaks in winter (2.44 °C), weakens in spring and autumn (both ~2.10 °C), and is lowest in summer (1.53 °C) (Fig. 5). Monthly values maximize in February (2.73 °C) and minimize in June (1.23 °C) (Fig. 4b). By inversion type, SBIs are consistently stronger than EIs: peak intensities reach 4.45 °C (SBI) versus 2.11 °C (EI) (Figs. 4e, 4h). Correspondingly, annual means rank SBI (3.02 °C) > all TI (2.13 °C) > EI (1.76 °C). The strongest seasonal maxima occur in winter in the Northwest for both overall TI (2.78 °C) and SBI (4.88 °C), while EI intensity peaks in winter in the South (2.43 °C). Notably, winter SBI strength exceeds EI by more than a factor of two. Geographically, SBI intensity varies substantially—annual means in northern and northwestern China are over twice those in the south—whereas EI strength is comparatively uniform, ranging from 1.63 °C (North/Northeast) to 1.93 °C (South), a spread of only 0.30 °C. Diurnally, TI, SBI, and EI intensities are generally higher at 08:00 BJT than at 20:00 (Figs. 4b, 4e, 4h). EI shows a regional reversal: daytime-stronger in the Northeast/North, but nighttime-stronger elsewhere. The maximum values by category occur at 08:00 in the Northwest for all TI (2.81 °C), 08:00 in the North for SBI (4.30 °C), and 20:00 in the South for EI (2.02 °C) (Tables SI, S2).





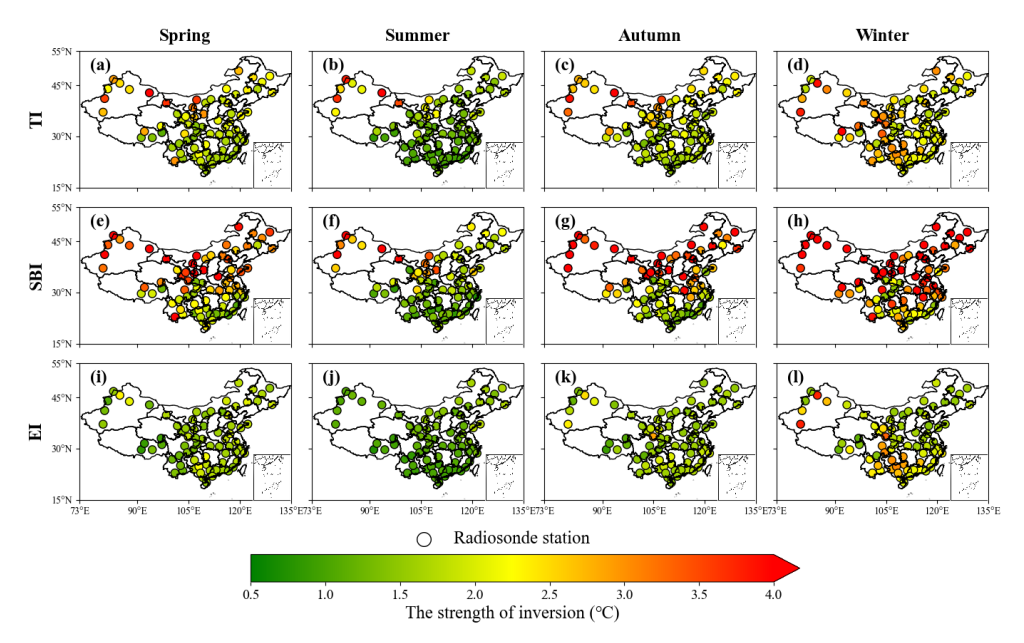


Fig.5 Spatial and seasonal distribution of inversion strength for different types of inversions.

4.1.3 Inversion thickness

Seasonal and regional patterns of inversion thickness for all TIs, SBIs, and EIs are shown in Figure 6 and summarized in Table 1. Across the 75 radiosonde stations, the annual mean thickness is 214 m. Layers sampled at 08:00 BJT are generally thicker than those at 20:00 BJT by about 40 m, consistent with the diurnal phasing of inversion intensity. Thickness varies markedly by season, maximizing in winter (231 m; Fig. 6d) and minimizing in summer (179 m; Fig. 6b). Monthly evolution follows a pronounced "V" shape (Fig. 4c), with a January peak of 243 m. By type, EIs are systematically thicker than SBIs, with annual means of 216 m and 201 m, respectively. Both exhibit winter maxima and summer minima. At 08:00, EI and SBI each display a clear "V"-shaped monthly cycle, whereas at 20:00 their behavior diverges: SBI thickness varies only modestly, while EI thickness remains comparatively stable across months (Figs. 4f, 4i). Spatially, inversion layers are thicker in the east and south—East, South, and Central China average 223 m—than in the north and west—Northeast, North, and Northwest average 209 m. South China shows the largest annual mean thickness (231 m), exceeding the national mean, whereas the Southwest has the thinnest layers (202 m). This pattern aligns with the regional predominance of inversion types: thicker EIs prevail in the eastern/southern regions, while thinner SBIs are more common in the western/northern regions. The lower overall inversion frequency in the Southwest, combined with the intrinsic thickness contrast between EI and SBI, further contributes to these regional differences.





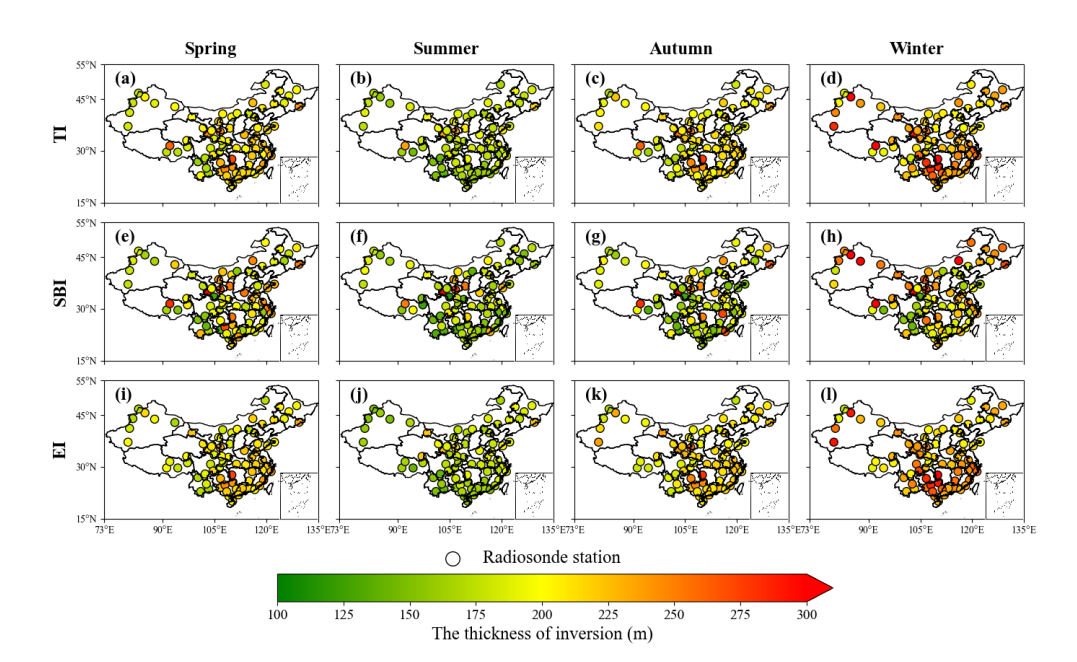


Fig.6 Spatial and seasonal distribution of inversion thickness for different types of inversions.

4.2 The correlation between temperature inversion and PM_{2.5}

4.2.1 Statistical relationship between temperature inversion and PM_{2.5} pollution events

We quantified the linkage between TIs and PM_{2.5} pollution by comparing the share of polluted days under inversion versus non-inversion conditions in each region (Table 2). At 08:00 BJT, a strong association emerges nationwide: co-occurrence rates span 84.6% in the Northeast (NE) to 62.9% in the Southwest (SW), indicating that morning pollution accumulation is substantially conditioned by inversions, with northern regions particularly sensitive—consistent with their higher prevalence of SBIs. By contrast, at 20:00 BJT the TI–PM_{2.5} coupling weakens markedly; the SW shows the lowest overlap, with only 27.7% of pollution events coinciding with inversions. This pronounced diurnal asymmetry suggests distinct formation regimes: daytime/morning pollution is frequently meteorology-limited by inversion trapping, whereas evening pollution is more strongly governed by emission timing and chemical processes than by boundary-layer stability.

Table 2. Frequency statistics of temperature inversion corresponding to PM2.5 pollution events in seven regions of China from 2016 to 2021.

	BJT 08:00				BJT 20:00				
Region Pollution	Inversion	No-	Inversion	Dallutian	Inversion	No-	Inversion		
		inversion	proportion	ronution		inversion	proportion		





1818	1489	329	81.9%	1713	1027	686	60.0%
3239	2672	567	82.5%	3004	1910	1094	63.6%
1749	1394	355	79.7%	1433	773	660	53.9%
1072	907	165	84.6%	709	480	229	67.7%
5409	4443	966	82.1%	4734	2299	2435	48.6%
1194	891	303	74.6%	881	464	417	52.7%
2523	1586	937	62.9%	2186	608	1578	27.7%
	3239 1749 1072 5409 1194	3239 2672 1749 1394 1072 907 5409 4443 1194 891	3239 2672 567 1749 1394 355 1072 907 165 5409 4443 966 1194 891 303	3239 2672 567 82.5% 1749 1394 355 79.7% 1072 907 165 84.6% 5409 4443 966 82.1% 1194 891 303 74.6%	3239 2672 567 82.5% 3004 1749 1394 355 79.7% 1433 1072 907 165 84.6% 709 5409 4443 966 82.1% 4734 1194 891 303 74.6% 881	3239 2672 567 82.5% 3004 1910 1749 1394 355 79.7% 1433 773 1072 907 165 84.6% 709 480 5409 4443 966 82.1% 4734 2299 1194 891 303 74.6% 881 464	3239 2672 567 82.5% 3004 1910 1094 1749 1394 355 79.7% 1433 773 660 1072 907 165 84.6% 709 480 229 5409 4443 966 82.1% 4734 2299 2435 1194 891 303 74.6% 881 464 417

Figure 7a reveals strong seasonal heterogeneity. Winter registers the most pollution events (17,540), exceeding spring, autumn, and summer by factors of 2.7, 3.2, and 13.8, respectively. Temperature inversions (TIs) substantially amplify this seasonal contrast: relative to no-inversion conditions, the probability of a pollution event rises by +52% in winter, +34% in autumn, +10% in spring, and is negligible in summer. The muted summer response likely reflects a shift toward ozone-dominated chemistry, weakening the coupling between $PM_{2.5}$ and inversion dynamics. Figure 7b shows that TIs not only increase occurrence but also severity—especially in winter—doubling extreme events (Level 4: $2\% \rightarrow 4\%$) and raising severe events (Level 3) by 3 percentage points ($15\% \rightarrow 18\%$). These observations are consistent with the inversion-driven explosive growth conceptual model for $PM_{2.5}$ (Zhong et al., 2017, 2018) and with the view that extreme haze is tightly linked to inversion meteorology (Yang and Shao, 2021). Autumn TIs exhibit a similar but weaker intensification (+3% in moderate/severe categories), whereas spring and summer TIs chiefly affect lower-severity bins. Collectively, the results establish TIs as a critical wintertime meteorological driver of both the frequency and intensity of haze in China.

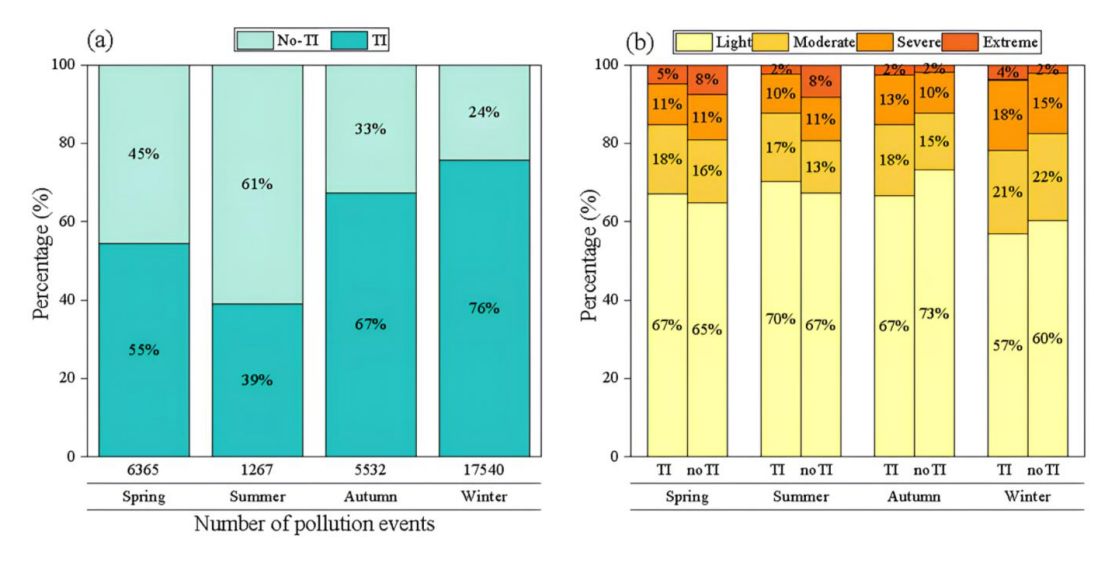


Fig. 7 (a) Frequency of inversion occurrence during polluted periods and (b) distribution of pollution levels in China (2016-2021).





4.2.2 Impacts of different TI types on PM_{2.5} concentrations

We quantify inversion impacts by contrasting mean PM_{2.5} under inversion and non-inversion conditions and assessing significance with two-sample *t*-tests for observations at 08:00 and 20:00 BJT (Fig. 8). In eastern China, results broadly align with Shao et al. (2023): PM_{2.5} increases significantly under inversions in the Northeast (NEC) and North China (NC), whereas South China (SC) exhibits significant decreases. In western China, most stations also show PM_{2.5} enhancements during inversions, with a notable exception at Hetian (southern Xinjiang), where spring–summer concentrations decline significantly (Figs. 8a, 8b). This anomaly likely reflects the dust-dominated composition of PM_{2.5} (>90%) and frequent spring–summer dust storms near the Taklamakan Desert; strong winds that accompany dust events are unfavorable for inversion formation, rendering dust outbreaks and inversion episodes largely mutually exclusive (Aishajiang et al., 2020). Consequently, during inversion periods, the dominant dust component is largely absent, yielding lower PM_{2.5}.

Disaggregating by inversion type reveals fundamentally different mechanisms. Surface-based inversions (SBIs) robustly increase PM_{2.5} across most regions—especially in winter and autumn (Figs. 8g, 8h)—consistent with nocturnal radiative cooling that produces a shallow, stable layer, suppresses vertical mixing, and accelerates near-surface accumulation (Stull, 1988; Zhong et al., 2017). The amplification in northern winters reflects longer nights and stronger surface cooling. By contrast, elevated inversions (EIs) exhibit spatially variable effects: they enhance PM_{2.5} in NEC, NC, and Northwest China (NWC), but reduce concentrations in SC. This pattern supports the hypothesis that EIs can inhibit pollutant transport (Yang and Shao, 2021): in SC, EIs often accompany synoptic subsidence or warm advection, establishing a capping layer that limits vertical exchange and isolates the region from northerly inflow. Such a transport-suppression mechanism is less relevant in northern China, where local emissions dominate. Diurnal contrasts further modulate these responses: morning (08:00) inversions generally exert stronger effects than evening (20:00) inversions, particularly in NWC (Figs. S8, S9). Occasional nighttime PM_{2.5} decreases under SBIs are observed at some NC/NEC stations, but these changes are not statistically significant.





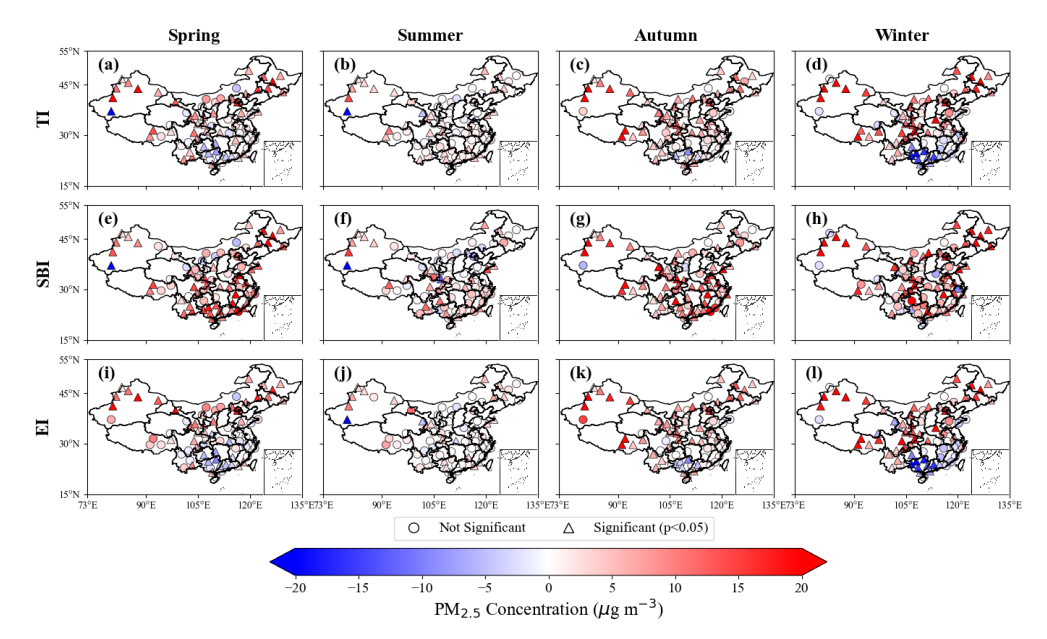


Fig. 8 Distribution of PM_{2.5} concentration differences with and without temperature inversion. The larger circle indicates significance at the 95% level (*t*-test)

We quantified PM_{2.5} responses to inversion parameters (strength, thickness) at 75 stations. Nationwide, PM_{2.5} rises near-linearly with inversion strength for both SBIs and EIs (Fig. 9h): below 8 °C, SBIs exert the stronger effect; above 8 °C, EIs become more influential. Regionally, four response regimes emerge: Northern Inland China, Southeastern Coastal China, Central China, and Southwestern China. In EC/SC, SBI intensity correlates positively with PM_{2.5} (R² > 0.9), whereas EI intensity correlates negatively (R² > 0.8); SBI strengths there seldom exceed 10 °C, far weaker than inland values. In NEC/NC, SBI strength can exceed 14 °C and is strongly coupled to PM_{2.5}. EI effects are mixed: NC shows a monotonic increase in PM_{2.5} with EI strength; NWC peaks at 10.9 °C (58.9 μg m⁻³) then declines; NEC shows no significant correlation. In the SWC, both SBI and EI display a parabolic relationship with PM_{2.5}, with SBI exerting the larger enhancement (correlation up to 0.94). In Central China, overall fits are poor/non-significant, likely reflecting (i) the limited sample (four stations) and (ii) the region's role as a convergence zone receiving substantial inflow from surrounding regions—regional transport contributes >65% to PM_{2.5} in cities such as Wuhan (Yu et al., 2020).

By contrast, inversion thickness shows a much weaker and less uniform association with $PM_{2.5}$ (Fig. S10). SBI thickness is generally positively correlated with $PM_{2.5}$ (except in NEC). For EI, significant thickness– $PM_{2.5}$ relationships appear only in NEC and NWC ($R^2 = 0.86$ and 0.92, respectively); elsewhere, EI thickness exerts negligible influence. Together, these results establish inversion strength—not thickness—as the dominant predictor of $PM_{2.5}$ accumulation (Fig. 9 vs. Fig. S10), consistent with the mechanism that a stronger temperature gradient yields greater static stability and more effective suppression of turbulent mixing (Liu et al., 2022)). Thickness primarily defines the volume of the trapping layer: a deep but weak inversion



340

341



can be eroded by mechanical turbulence more readily than a shallow but intense one.

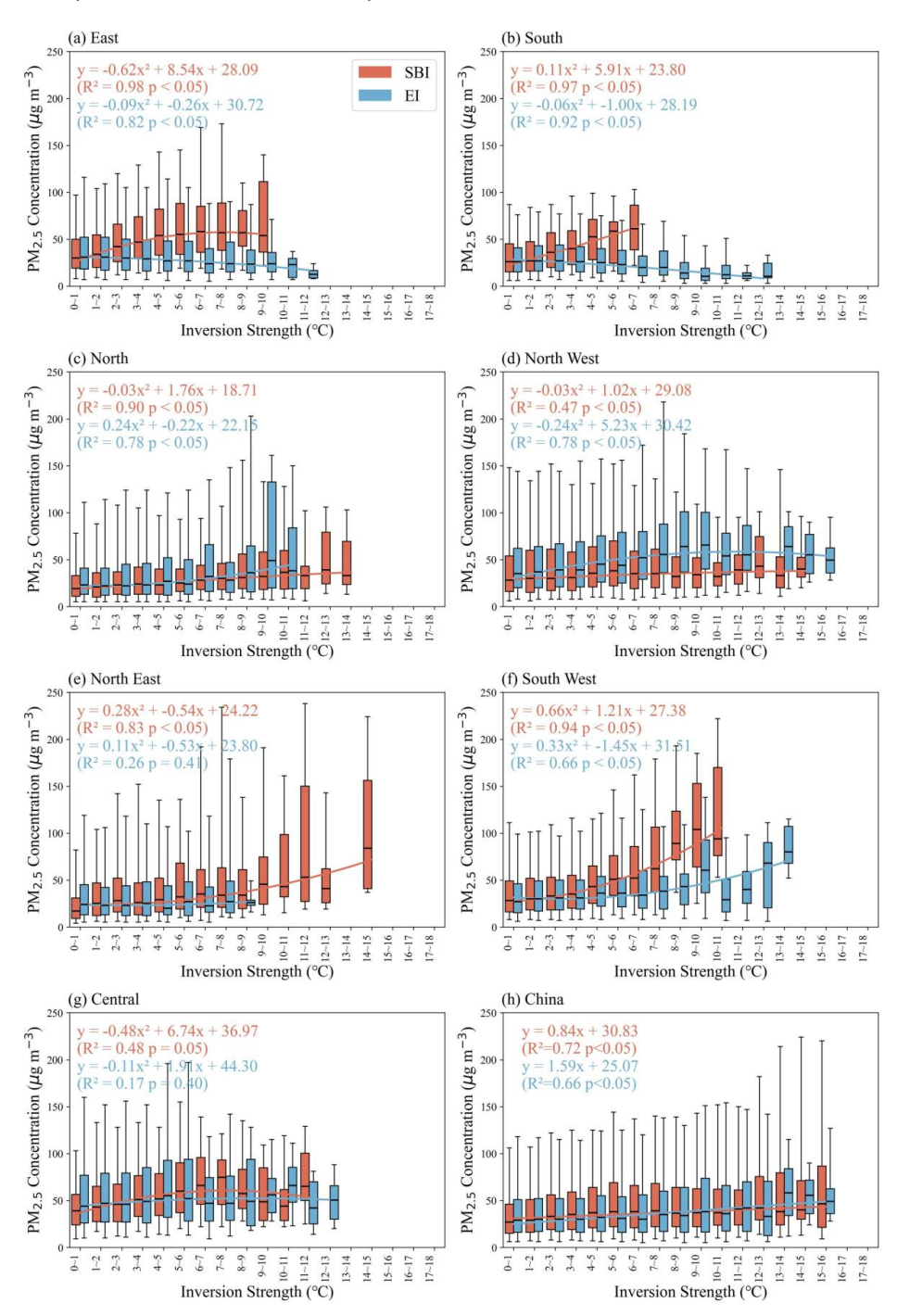


Figure.9 Fitting relationship between inversion strength and PM_{2.5} concentration across seven regions of China from 2016 to 2021. The ends of the boxes, the ends of the bars, and the short line across each box represent the 25th and 75th percentiles, the 5th and 95th percentiles, and the median, respectively. Each strength interval contains a sample size ≥ 10 .



343344

345

346

347

348

349

350

351

352

353

354

355

356

357

358

359

360

361

362

363

364

365366

367

368

369

370

371

372



5 Conclusions

Temperature inversions (TIs) are widely recognized as a key meteorological regulator of near-surface PM2.5, yet their nationwide behaviour and impacts have remained incompletely characterized. Leveraging high-vertical-resolution radiosondes from 75 stations (2016-2021) and collocated surface PM2.5, we provide an observation-based assessment of inversion frequency, intensity, thickness, and diurnal variability across China, and quantify how distinct inversion types modulate pollution accumulation. First, TIs are pervasive: the national annual means are 51.8% for frequency, 2.13 °C for strength, and 214 m for thickness. Strong regional heterogeneity emerges. SBIs occur more frequently and are substantially stronger over inland northern regions (annual mean 3.02 °C), whereas EIs prevail along the southeastern coast and are thicker (e.g., 235 m in Central China; 227 m in South China). Low-level inversions are comparatively rare in the Southwest. Diurnally, inversions are more frequent, stronger, and thicker at 08:00 BJT than at 20:00, with the SBI day-night contrast muted in summer and amplified in winter consistent with radiative control. Second, TIs materially elevate winter haze risk. Relative to non-inversion conditions, the probability of a pollution event increases by 52% in winter, and the share of extreme events doubles, establishing TIs as a firstorder meteorological driver of both frequency and severity of winter haze in China. Third, the type of inversion matters. SBIs robustly enhance PM_{2.5} across most regions, reflecting efficient near-surface trapping under nocturnal stability. EIs show regionally divergent behaviour: they enhance PM_{2.5} in the north and northwest but are negatively associated with PM_{2.5} in the east and south, consistent with a transport-inhibition mechanism that limits northerly inflow under subsidence/warm-advection regimes. Fourth, inversion strength is the dominant predictor of PM2.5 accumulation, while thickness plays a secondary, regiondependent role. Nationally, PM2.5 increases near-linearly with intensity for both SBI and EI; below 8 °C SBI effects dominate, whereas above 8 °C EI effects strengthen. Thickness is generally weakly correlated with PM_{2.5}, except in select regions (e.g., NEC/NWC for EI), underscoring that static stability (temperature gradient) governs ventilation more directly than layer depth. These findings offer concrete avenues for forecasting and control. (i) Incorporating real-time inversion diagnostics especially intensity—into operational air-quality models should improve short-lead PM_{2.5} forecasts and early-warning skill, particularly in winter. (ii) Region-specific strategies are warranted: curbing evening-night emissions and promoting nocturnal ventilation are likely most effective where SBIs dominate (northern basins/plains), whereas transport management and synoptic-regime awareness may be more impactful in the southeast where EIs can isolate the boundary layer from upwind inflow. (iii) The observed diurnal asymmetry suggests targeted mitigation during windows of maximum trapping (pre-sunrise to morning transition). Our assessment remains limited by sparser coverage over plateau terrain and the lack of vertical PM2.5 profiles, which constrains diagnosis of aerosol layering and entrainment. Future work should augment radiosondes with Raman/HSRL lidar,

UAV or aircraft soundings, and assimilate inversion-aware stability metrics into kilometre-scale chemical transport models;





374 emissions, and climate-driven shifts in nocturnal cooling and synoptic patterns. These steps will sharpen causal attribution of 375 TI-pollution coupling and strengthen the forecast-to-policy pipeline for region-tailored air-quality management. 376 377 Data availability. The radiosonde data used in this study are available from the China Meteorological Administration (CMA). 378 The hourly ground-level PM_{2.5} concentration data can be obtained from the China National Environmental Monitoring Centre 379 (CNEMC; real-time platform: https://www.cnemc.cn/en/). 380 381 Author contributions. YF and HW designed the study. HH, JG, XZ and FM contributed to the observation data, provided 382 experimental assistance, and analyzed the methodology. YF wrote the paper with input from all the other authors. 383 384 Competing interests. The authors declare that they have no known competing financial interests or personal relationships that 385 could have appeared to influence the work reported in this paper. 386 387 Acknowledgements. This study was funded by the Key Laboratory of Atmosphere Sounding, China Meteorological 388 Administration (2023KLAS12M). 389 390 Financial support. This research has been supported by the Key Laboratory of Atmosphere Sounding, China Meteorological 391 Administration (2023KLAS12M). 392 393 References 394 Aishajiang, A., Liang, F., Xu, H., Muhetaer, W., and Maimaitiaili, M.: Transport pathway of dust storm and its impact on air quality in Hetian Oasis, Acta Scientiae Circumstantiae, 40, https://doi.org/10.13671/j.hjkxxb.2020.0159, 2020. 395 396 Chan, C. K. and Yao, X.: Air pollution in mega cities in China, Atmospheric Environment, 42, 1-42, 397 https://doi.org/10.1016/j.atmosenv.2007.09.003, 2008. 398 Chen, J., Lv, H., Wang, Q., Wang, G., Jia, K., Zhao, C., Shi, W., and Yan, X.: Revolutionizing Satellite Real-Time Air Pollution 399 Alerts through New On-Orbit System-on-Chip Technology, Environ. Sci. Technol., 59, https://doi.org/10.1021/acs.est.5c02470, 400 2025. 401 Czarnecka, M., Nidzgorska-Lencewicz, J., and Rawicki, K.: Temporal structure of thermal inversions in Leba (Poland), Theor Appl Climatol, 136, 1–13, https://doi.org/10.1007/s00704-018-2459-8, 2019. 402 403 Deng, C., Qin, C., Li, Z., and Li, K.: Spatiotemporal variations of PM_{2.5} pollution and its dynamic relationships with 404 meteorological conditions beijing-tianjin-hebei region, Chemosphere, 301, 134640,

leverage geostationary multi-sensor diurnal sampling to resolve inversion evolution; and evaluate co-trends among inversions,





- 405 https://doi.org/10.1016/j.chemosphere.2022.134640, 2022.
- 406 Feng, X., Wei, S., and Wang, S.: Temperature inversions in the atmospheric boundary layer and lower troposphere over the
- 407 Sichuan Basin, China: Climatology and impacts on air pollution, Science of The Total Environment, 726, 138579,
- 408 https://doi.org/10.1016/j.scitotenv.2020.138579, 2020.
- 409 Garcia, A., Santa-Helena, E., De Falco, A., De Paula Ribeiro, J., Gioda, A., and Gioda, C. R.: Toxicological Effects of Fine
- 410 Particulate Matter (PM2.5): Health Risks and Associated Systemic Injuries—Systematic Review, Water Air Soil Pollut, 234,
- 411 https://doi.org/10.1007/s11270-023-06278-9, 2023.
- 412 Guo, J., Miao, Y., Zhang, Y., Liu, H., Li, Z., Zhang, W., He, J., Lou, M., Yan, Y., Bian, L., and Zhai, P.: The climatology of
- 413 planetary boundary layer height in China derived from radiosonde and reanalysis data, Atmos. Chem. Phys., 16, 13309–13319,
- 414 https://doi.org/10.5194/acp-16-13309-2016, 2016.
- 415 Guo, J., Chen, X., Su, T., Liu, L., Zheng, Y., Chen, D., Li, J., Xu, H., Lv, Y., He, B., Li, Y., Hu, X.-M., Ding, A., and Zhai, P.:
- 416 The Climatology of Lower Tropospheric Temperature Inversions in China from Radiosonde Measurements: Roles of Black
- 417 Carbon, Local Meteorology, and Large-Scale Subsidence, Journal of Climate, 33, 9327–9350, https://doi.org/10.1175/JCLI-
- 418 D-19-0278.1, 2020.
- 419 Huang, Q., Chu, Y., and Li, Q.: Climatology of low-level temperature inversions over China based on high-resolution
- 420 radiosonde measurements, Theor Appl Climatol, 144, 415–429, https://doi.org/10.1007/s00704-021-03536-w, 2021.
- 421 Kahl, J. D.: Characteristics of the low-level temperature inversion along the Alaskan Arctic coast, Intl Journal of Climatology,
- 422 10, 537–548, https://doi.org/10.1002/joc.3370100509, 1990.
- 423 Kahl, J. D. W., Martinez, D. A., and Zaitseva, N. A.: Long-term variability in the low-level inversion layer over the arctic
- 424 ocean, Int. J. Climatol., 16, 1297-1313, https://doi.org/10.1002/(SICI)1097-0088(199611)16:11%253C1297::AID-
- 425 JOC86%253E3.0.CO;2-T, 1996.
- 426 Kassomenos, P. A., Paschalidou, A. K., Lykoudis, S., and Koletsis, I.: Temperature inversion characteristics in relation to
- 427 synoptic circulation above Athens, Greece, Environ Monit Assess, 186, 3495–3502, https://doi.org/10.1007/s10661-014-3632-
- 428 x, 2014.
- 429 Lagmiri, S. and Dahech, S.: Temperature Inversion and Particulate Matter Concentration in the Low Troposphere of Cergy-
- 430 Pontoise (Parisian Region), Atmosphere, 15, 349, https://doi.org/10.3390/atmos15030349, 2024.
- 431 Largeron, Y. and Staquet, C.: Persistent inversion dynamics and wintertime PM₁₀ air pollution in Alpine valleys, Atmospheric
- 432 Environment, 135, 92–108, https://doi.org/10.1016/j.atmosenv.2016.03.045, 2016.
- 433 Li, J., Chen, H., Li, Z., Wang, P., Fan, X., He, W., and Zhang, J.: Analysis of Low-level Temperature Inversions and Their
- 434 Effects on Aerosols in the Lower Atmosphere, Adv. Atmos. Sci., 36, 1235-1250, https://doi.org/10.1007/s00376-019-9018-9,
- 435 2019
- 436 Li, Y., Yan, J., and Sui, X.: Tropospheric temperature inversion over central China, Atmospheric Research, 116, 105-115,
- 437 https://doi.org/10.1016/j.atmosres.2012.03.009, 2012.
- 438 Liang, C., Zang, Z., Li, Z., and Yan, X.: An Improved Global Land Anthropogenic Aerosol Product Based on Satellite
- 439 Retrievals From 2008 to 2016, IEEE Geosci. Remote Sensing Lett., 18, 944–948, https://doi.org/10.1109/LGRS.2020.2991730,
- 440 2021
- 441 Liu, B., Ma, X., Ma, Y., Li, H., Jin, S., Fan, R., and Gong, W.: The relationship between atmospheric boundary layer and





- 442 temperature inversion layer and their aerosol capture capabilities, Atmospheric Research, 271, 106121,
- 443 https://doi.org/10.1016/j.atmosres.2022.106121, 2022.
- 444 Luo, N., Zhang, Y., Jiang, Y., Zuo, C., Chen, J., Zhao, W., Shi, W., and Yan, X.: Unveiling global land fine- and coarse-mode
- 445 aerosol dynamics from 2005 to 2020 using enhanced satellite-based monthly inversion data, Environmental Pollution,
- 446 https://doi.org/10.1016/j.envpol.2024.123838, 2024.
- 447 Ma, Y., Yao, W., and Huang, B.: Comparison of temperature and geopotential height records between 59 type and L-band
- 448 radiosonde systems, Journal of Applied Meteorological Science, 21, 214-220, https://doi.org/10.3969/j.issn.1001-
- 449 7313.2010.02.011, 2010.
- 450 Meng, X., Wei, Z., and Ye, C.: Variation Characteristics of Ambient Air Quality in China during 2013-2022, Environmental
- 451 Monitoring and Forewarning, 15, 1–7, https://doi.org/10.3969/j.issn.1674-6732.02023.05.001, 2023.
- 452 Miao, Y., Che, H., Zhang, X., and Liu, S.: Integrated impacts of synoptic forcing and aerosol radiative effect on boundary layer
- 453 and pollution in the Beijing-Tianjin-Hebei region, China, Atmospheric Chemistry and Physics, 20, 5899-5909,
- 454 https://doi.org/10.5194/acp-20-5899-2020, 2020.
- 455 Milionis, A. E. and Davies, T. D.: A five-year climatology of elevated inversions at Hemsby (UK), Intl Journal of Climatology,
- 456 12, 205–215, https://doi.org/10.1002/joc.3370120209, 1992.
- 457 Ministry of ecology and environment the people's republic of China: Report on the State of the Ecology and Environment in
- China 2022, Ministry of ecology and environment the people's republic of China, 72 pp., 2022.
- 459 Morawska, L., Zhu, T., Liu, N., Amouei Torkmahalleh, M., De Fatima Andrade, M., Barratt, B., Broomandi, P., Buonanno, G.,
- 460 Carlos Belalcazar Ceron, L., Chen, J., Cheng, Y., Evans, G., Gavidia, M., Guo, H., Hanigan, I., Hu, M., Jeong, C. H., Kelly,
- 461 F., Gallardo, L., Kumar, P., Lyu, X., Mullins, B. J., Nordstrøm, C., Pereira, G., Querol, X., Yezid Rojas Roa, N., Russell, A.,
- Thompson, H., Wang, H., Wang, L., Wang, T., Wierzbicka, A., Xue, T., and Ye, C.: The state of science on severe air pollution
- 463 episodes: Quantitative and qualitative analysis, Environment International, 156, 106732,
- 464 https://doi.org/10.1016/j.envint.2021.106732, 2021.
- 465 Palarz, A., Celiński-Mysław, D., and Ustrnul, Z.: Temporal and spatial variability of surface-based inversions over Europe
- 466 based on ERA -Interim reanalysis, Intl Journal of Climatology, 38, 158-168, https://doi.org/10.1002/joc.5167, 2018.
- 467 Peng, Y., Zhao, Y., Gao, N., Sheng, D., Tang, S., Zheng, S., and Wang, M.: Spatiotemporal evolution of PM_{2.5} and its
- 468 components and drivers in China, 2000-2023: effects of air pollution prevention and control actions in China, Environmental
- 469 Geochemistry and Health, 47, 69, https://doi.org/10.1007/s10653-025-02375-2, 2025.
- 470 Rendón, A. M., Salazar, J. F., Palacio, C. A., and Wirth, V.: Temperature Inversion Breakup with Impacts on Air Quality in
- 471 Urban Valleys Influenced by Topographic Shading, Journal of Applied Meteorology and Climatology, 54, 302-321,
- 472 https://doi.org/10.1175/JAMC-D-14-0111.1, 2015.
- 473 Rentschler, J. and Leonova, N.: Global air pollution exposure and poverty, Nat Commun, 14, 4432,
- 474 https://doi.org/10.1038/s41467-023-39797-4, 2023.
- 475 Schiemann, Luethi, and Schaer: Seasonality and Interannual Variability of the Westerly Jet in the Tibetan Plateau Region,
- 476 Journal of climate, 22, 2009.
- 477 Serreze, M., Kahl, J., and Schnell, R.: Low-Level Temperature Inversions of the Eurasian Arctic and Comparisons with Soviet
- 478 Drifting Station Data, Journal of Climate, 5, 615-629, https://doi.org/10.1175/1520-





- 479 0442(1992)005%3C0615:LLTIOT%3E2.0.CO;2, 1992.
- 480 Shao, M., Xu, X., Lu, Y., and Dai, Q.: Spatio-temporally differentiated impacts of temperature inversion on surface PM_{2.5} in
- 481 eastern China, Science of The Total Environment, 855, 158785, https://doi.org/10.1016/j.scitotenv.2022.158785, 2023.
- 482 Stull, R. B.: An Introduction to Boundary Layer Meteorology, Springer Netherlands, 1988.
- 483 Sun, M., Xie, Z., Yao, X., Wang, S., and Dong, L.: Multilayer temperature inversion structures and their potential impact on
- 484 atmospheric pollution in northwest China, Atmospheric Environment, 343, 120998,
- 485 https://doi.org/10.1016/j.atmosenv.2024.120998, 2025.
- 486 Vihma, T., Kilpeläinen, T., Manninen, M., Sjöblom, A., Jakobson, E., Palo, T., Jaagus, J., and Maturilli, M.: Characteristics of
- 487 Temperature and Humidity Inversions and Low-Level Jets over Svalbard Fjords in Spring, Advances in Meteorology, 2011,
- 488 1–14, https://doi.org/10.1155/2011/486807, 2011.
- 489 Wallace, J. and Kanaroglou, P.: The effect of temperature inversions on ground-level nitrogen dioxide (NO2) and fine
- 490 particulate matter (PM_{2.5}) using temperature profiles from the Atmospheric Infrared Sounder (AIRS), Science of The Total
- 491 Environment, 407, 5085–5095, https://doi.org/10.1016/j.scitotenv.2009.05.050, 2009.
- 492 WHO: WHO global air quality guidelines: particulate matter (PM_{2.5} and PM₁₀), ozone, nitrogen dioxide, sulfur dioxide and
- 493 carbon monoxide, 2021.
- 494 Wolf, T., Esau, I., and Reuder, J.: Analysis of the vertical temperature structure in the Bergen valley, Norway, and its connection
- 495 to pollution episodes, J. Geophys. Res. Atmos., 119, https://doi.org/10.1002/2014JD022085, 2014.
- 496 Wu, W., Zha, Y., Zhang, J., Gao, J., and He, J.: A temperature inversion-induced air pollution process as analyzed from Mie
- 497 LiDAR data, Science of The Total Environment, 479–480, 102–108, https://doi.org/10.1016/j.scitotenv.2014.01.112, 2014.
- 498 Xu, T., Song, Y., Liu, M., Cai, X., Zhang, H., Guo, J., and Zhu, T.: Temperature inversions in severe polluted days derived
- 499 from radiosonde data in North China from 2011 to 2016, Science of The Total Environment, 647, 1011-1020,
- 500 https://doi.org/10.1016/j.scitotenv.2018.08.088, 2019.
- Xu, T., Liu, B., Zhang, M., Song, Y., Kang, L., Wang, T., Liu, M., Cai, X., Zhang, H., and Zhu, T.: Temperature inversions in
- 502 China derived from sounding data from 1976 to 2015, Tellus B: Chemical and Physical Meteorology, 73, 1898906,
- 503 https://doi.org/10.1080/16000889.2021.1898906, 2021.
- 504 Yan, X., Liang, C., Jiang, Y., Luo, N., Zang, Z., and Li, Z.: A Deep Learning Approach to Improve the Retrieval of Temperature
- and Humidity Profiles From a Ground-Based Microwave Radiometer, IEEE Trans. Geosci. Remote Sensing, 58, 8427–8437,
- 506 https://doi.org/10.1109/TGRS.2020.2987896, 2020.
- 507 Yan, X., Zang, Z., Jiang, Y., Shi, W., Guo, Y., Li, D., Zhao, C., and Husi, L.: A Spatial-Temporal Interpretable Deep Learning
- 508 Model for improving interpretability and predictive accuracy of satellite-based PM_{2.5}, Environmental Pollution, 273, 116459,
- 509 https://doi.org/10.1016/j.envpol.2021.116459, 2021.
- 510 Yan, X., Zuo, C., Li, Z., Chen, H. W., Jiang, Y., He, B., Liu, H., Chen, J., and Shi, W.: Cooperative simultaneous inversion of
- 511 satellite-based real-time PM_{2.5} and ozone levels using an improved deep learning model with attention mechanism,
- 512 Environmental Pollution, 327, 121509, https://doi.org/10.1016/j.envpol.2023.121509, 2023.
- 513 Yang, J. and Shao, M.: Impacts of Extreme Air Pollution Meteorology on Air Quality in China, JGR Atmospheres, 126,
- 514 e2020JD033210, https://doi.org/10.1029/2020JD033210, 2021.

https://doi.org/10.5194/egusphere-2025-4751 Preprint. Discussion started: 28 October 2025 © Author(s) 2025. CC BY 4.0 License.





- 515 Yang, Y., Li, Z., Guo, J., Wang, Y., Wu, H., Shang, Y., Wang, Y., Zhu, L., and Yan, X.: Revolutionizing Clear-Sky Humidity
- 516 Profile Retrieval with Multi-Angle-Aware Networks for Ground-Based Microwave Radiometers, J Remote Sens, 5, 0736,
- 517 https://doi.org/10.34133/remotesensing.0736, 2025.
- 518 Yin, P.-Y., Chang, R.-I., Day, R.-F., Lin, Y.-C., and Hu, C.-Y.: Improving PM_{2.5} Concentration Forecast with the Identification
- of Temperature Inversion, Applied Sciences, 12, 71, https://doi.org/10.3390/app12010071, 2021.
- 520 Yu, C., Zhao, T., Bai, Y., Zhang, L., Kong, S., Yu, X., He, J., Cui, C., Yang, J., You, Y., Ma, G., Wu, M., and Chang, J.: Heavy
- 521 air pollution with a unique "non-stagnant" atmospheric boundary layer in the Yangtze River middle basin aggravated by
- 522 regional transport of PM_{2.5} over China, Atmospheric Chemistry and Physics, 20, 7217–7230, https://doi.org/10.5194/acp-20-
- 523 7217-2020, 2020.
- 524 Zang, Z., Wang, W., You, W., Li, Y., Ye, F., and Wang, C.: Estimating ground-level PM_{2.5} concentrations in Beijing, China
- 525 using aerosol optical depth and parameters of the temperature inversion layer, Science of The Total Environment, 575, 1219-
- 526 1227, https://doi.org/10.1016/j.scitotenv.2016.09.186, 2017.
- 527 Zang, Z., Li, D., Guo, Y., Shi, W., and Yan, X.: Superior PM_{2.5} Estimation by Integrating Aerosol Fine Mode Data from the
- 528 Himawari-8 Satellite in Deep and Classical Machine Learning Models, Science of The Total Environment, 13, 2775,
- 529 https://doi.org/10.3390/rs13142779, 2021.
- 530 Zhang, J., Zheng, Y., Li, Z., Xia, X., and Chen, H.: A 17-year climatology of temperature inversions above clouds over the
- 531 ARM SGP site: The roles of cloud radiative effects, Atmospheric Research, 237, 104810,
- 532 https://doi.org/10.1016/j.atmosres.2019.104810, 2020.
- 533 Zhang, Y. H., Zhang, S. D., Yi, F., and Chen, Z. Y.: Statistics of lower tropospheric inversions over the continental United
- 534 States, Ann. Geophys., 29, 401–410, https://doi.org/10.5194/angeo-29-401-2011, 2011.
- 535 Zhong, J., Zhang, X., Wang, Y., Sun, J., Zhang, Y., Wang, J., Tan, K., Shen, X., Che, H., Zhang, L., Zhang, Z., Qi, X., Zhao,
- 536 H., Ren, S., and Li, Y.: Relative contributions of boundary-layer meteorological factors to the explosive growth of PM_{2.5} during
- 537 the red-alert heavy pollution episodes in Beijing in December 2016, J Meteorol Res, 31, 809-819,
- 538 https://doi.org/10.1007/s13351-017-7088-0, 2017.
- 539 Zhong, J., Zhang, X., Dong, Y., Wang, Y., Liu, C., Wang, J., Zhang, Y., and Che, H.: Feedback effects of boundary-layer
- 540 meteorological factors on cumulative explosive growth of PM_{2.5} during winter heavy pollution episodes in Beijing from 2013
- 541 to 2016, Atmos. Chem. Phys., 18, 247–258, https://doi.org/10.5194/acp-18-247-2018, 2018.
- 542 Zou, J., Chen, H. W., Li, H., Wang, Q., Wang, G., Jia, K., Chen, Z., Zhao, C., Shi, W., Yang, Y., Tang, Y., Chen, J., Zhang, Y.,
- 543 Xu, T., Wang, Y., Liu, G., and Yan, X.: Amplified urban heat island effect in southern china's old towns following atmospheric
- 544 regulation policies, Sustainable Cities and Society, 131, 106675, https://doi.org/10.1016/j.scs.2025.106675, 2025.
- 545 Zuo, C., Chen, J., Zhang, Y., Jiang, Y., Liu, M., Liu, H., Zhao, W., and Yan, X.: Evaluation of four meteorological reanalysis
- 546 datasets for satellite-based PM_{2.5} retrieval over China, Atmospheric Environment, 305, 119795,
- 547 https://doi.org/10.1016/j.atmosenv.2023.119795, 2023.